Towards Automatic Control of Scanning Transmission Electron Microscopes

Arturo Tejada, Saartje W. van der Hoeven, Arnold J. den Dekker, and Paul M. J. Van den Hof

***Abstract*— Scanning transmission electron microscopes are the tools of choice for material science research, since they provide information on the internal structure of a wide range of specimens. These sophisticated machines are operated manually by skilled technicians, who execute complex and repetitive procedures, such as measuring nano-particles, using mainly visual feedback. Hence, there is a need for new global control strategies to automate these procedures. These strategies, however, must be based on a firm understanding of the microscopes from the system theoretical perspective. To the best of our knowledge, such perspective is lacking in the literature. Thus, it is provided here through a new modeling framework that facilitates the future development of global control strategies. The paper also aims to introduce scanning transmission electron microscopy as an important and untapped area of application for control engineers.**

I. Introduction

Scanning transmission electron microscopes, denoted STEMs, are the tools of choice for material science research since they can reveal information about the internal structure of a wide range of specimens, with high magnification. Their images are derived from the diffraction patterns generated by the scattering of an electron beam by a specimen. Acquiring and interpreting these images, however, is not a trivial task. Since the STEMs combine the best features of the two basic types of electron microscopes (the scanning and the transmission electron microscopes), there is a large amount of (microscope) settings and physical parameters that must be taken into account while acquiring images. Moreover, successful STEM operation requires knowledge of the physics of the beam-specimen interaction (different specimens yield different diffraction patterns), a clear understanding of the behavior of the particular microscope taking the images, and experience fine-tuning it. Hence, electron microscope operators are highly trained individuals, who invariably operate the microscopes manually, using direct visual interpretation of the images produced by the microscope. Evidently, this makes it impossible to attain consistent image quality across different operators [1].

Integrating this expertise into automation algorithms is a challenging task. Several algorithms are available to automate operations such as microscope alignment or astigmatism correction [2]–[5]. However, they are not accurate enough and still require further manual adjustments [1]. In addition, most of these methods are based on qualitative image analysis. Quantitative analysis methods are lacking. More importantly, a systematic use of control theory concepts is also lacking. Control loops are only used locally in the microscope's main components (e.g., the electromagnetic lenses). However, the microscope at large is treated as an interconnection of 'open-loop' components, each of which is improved individually. Algorithms for global procedures (i.e. procedures that coordinate several STEM components) such as maintaining image quality, automatically finding and measuring features of interest in specimens, or automating repetitive tasks are not available. Unfortunately, these algorithms cannot be developed without a firm understanding of the STEMs from a system theoretical perspective. To the best of our knowledge, this perspective is not present in the literature. This, perhaps, may have been caused by the fact that the control community, with a few exceptions [6], has not been made aware of this area of application.

Thus, this paper aims to provide such perspective by introducing a framework from which dynamical models adequate for the analysis and control of STEMs can be derived. This framework provides insight into the identification tasks and control strategies needed for automating two important global procedures: microscope alignment and coordinated position control. Moreover, through this presentation, the paper also aims to introduce STEMs as an important and untapped area of application for control engineers. These ideas were developed in the framework of the CONDOR project, which is managed by the Embedded Systems Institute (`www.esi.nl`) and seeks to transform the traditional STEMs from qualitative imaging instruments into flexible quantitative nano-measurement tools.

The rest of the paper is organized as follows: Section II summarizes the STEM principle of operation. Section III describes the aforesaid global procedures: microscope alignment and coordinated position control. The new STEM modeling framework is introduced in Section IV, which also identifies the main challenges for automation. Finally, Section V contains our conclusions.

II. STEM Operation

This section is divided into two parts. The first one describes the STEM principle of operation, emphasizing only the main STEM components. The second part summarizes the physics of image formation, which is the basis for the modeling framework introduced in Section IV.

A. *Principle of Operation*

STEMs were introduced in 1968 by A. Crewe and coworkers [7]. Based on Figure 1, their principle of operation can

The authors are affiliated with the Delft Center for Systems and Control at the Delft University of Technology, The Netherlands.

be summarized as follows [8]: An electron source (usually a field emission gun or FEG) generates an electron beam that is focused by the joint action of a condenser lens and an objective lens (denoted CL and UOL) to form a demagnified image of the electron source (called probe) at a specimen. The electrons that go through the specimen and are scattered at high angles are subsequently 'counted' by a detector (HAADF in Figure 1), which generates an 'intensity' signal proportional to the number of detected electrons. The final image is created by sweeping the probe over the specimen in a raster pattern, by means of deflector coils, and plotting the electron intensity as a function of the probe's position on a computer screen.

The electrons leave the FEG with energy $E = eU$ set by the FEG's accelerating voltage U (e is the electron charge), and travel in directions almost parallel to the optical axis (the z-axis in Figure 1). They are then focused by electromagnetic lenses, which are composed of coils enclosed by round symmetric soft iron pole pieces [9]. Each lens behavior mimics that of an optical thin lens with adjustable focal distance $f(t)$. The later is measured with respect to an arbitrary fixed point in the lens structure and is adjusted by varying the current $i_L(t)$ applied to the coil since [10],

$$\frac{1}{f(t)} = \kappa \frac{i_L^2(t)}{U}, \tag{1}$$

where κ is a lens-dependent proportionality constant.

The objective lens pole piece is divided into two sections, and is conceptually represented as two separate lenses: the upper objective lens (UOL) and the lower objective lens (LOL). While the UOL focuses the probe on the specimen, the LOL collects the diffracted electrons and forms a diffraction pattern (DP) on its back focal plane. The latter is generally located a few millimeters beneath the lens. Thus, most STEMs use a combination of intermediate and projection lenses (denoted IL and PL) to shift the DP to a lower plane where detectors, such as the high angular annular dark field detector (HAADF), are located. Alternatively, these lenses can be set to project the DP on a computer screen using a CCD camera, or to project, with the aid of an additional probe lens (PrL), an image of the probe.

Note that the objective lens is said to be 'in focus' when its focal distance, $f(t)$, matches the distance Z_{ref} between the lens' fixed point and the specimen surface. The specimen has an average thickness of 5nm to 500nm [9] and is placed on a specimen holder (called goniometer) that lies between the UOL and the LOL. The goniometer is a mechanism that permits the specimen translation in the three cartesian axes (± 1.5mm) and its rotation in the roll and yaw axes (up to $\pm 60°$). Note, however, that probe's $x - y$ position on the specimen (with respect to the optical axis) is determined by the deflector coils (see Subsection III-B).

To conclude, note that in a STEM the image resolution is determined by the 'quality' of the probe, which is influenced mainly by the properties of the FEG and the aberrations of the objective lens [10]. Also note that the image magnification is determined by the size of the raster pattern [11].

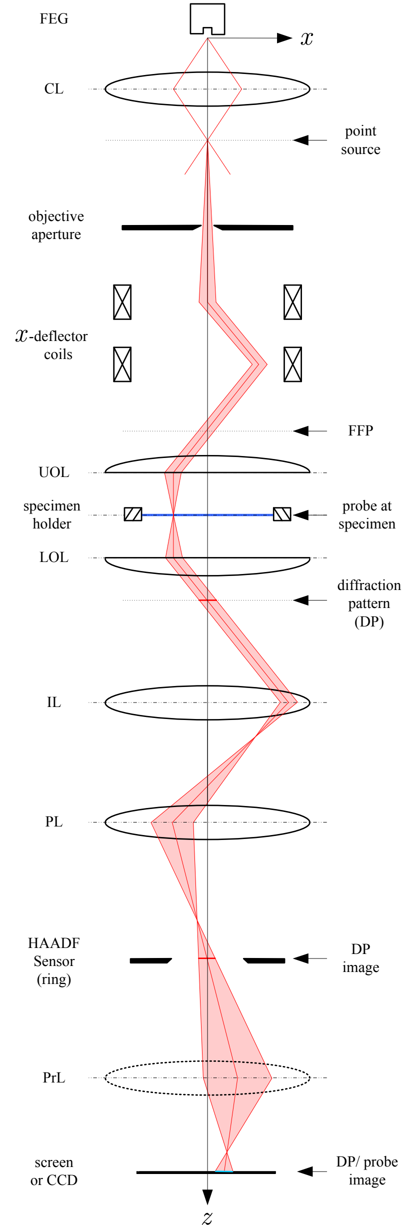

Fig. 1. Main STEM components. The central ray diagram illustrates the image formation process. The angles are greatly exaggerated. In practice they span only a few miliradians.

For instance, a raster pattern of 1μm $\times$ 1μm projected on a 10cm $\times$ 10cm screen yields a magnification of 10^5.

B. Image Formation Process

The formal description of the STEM image formation process can be found in, for instance, [12]. Here, only a summary is offered. Images are time-varying, real-valued (intensity) functions $I : \mathbb{R}^2 \times \mathbb{R} \to \mathbb{R}$, with action $I : (r,t) \mapsto I(r,t)$ or $I : (q,t) \mapsto I(q,t)$ depending on whether I denotes a real space image or a frequency space image, where $r, q \in \mathbb{R}^2$, and $t \in \mathbb{R}^+$ denotes time. All images are formed on an $x - y$ plane perpendicular to the optical axis under the following standard assumptions [10].

Asumption 2.1: (a) The FEG is an ideal point source of electrons. (b) All lenses, except the objective lens, are ideal. (c) The specimen is thin.

These assumptions simplify the mathematical derivations without modifying the principles of image formation (see [10] for more details). Assumption 2.1(a) implies that all electrons in the beam come from the same point in space and have the same energy (hence, U is a constant). Assumption 2.1(b) implies that only the aberrations of the objective lens are important, which is the case in practice. This assumption also implies that the crossover image after the CL is an ideal point source (see Figure 1). Finally, Assumption 2.1(c) allows the specimen to be treated as a phase object [10].

The electrons emanating from the crossover are diffracted by the objective aperture. Thus, the probe has finite width and an associated wave function, $p(r,t)$, given by [8]

$$p(r,t) = \mathfrak{F}^{-1}\{A(q)\exp(j\chi(q,t))\}. \tag{2}$$

In this equation, $\mathfrak{F}$ denotes the Fourier transform over r, $j = \sqrt{-1}$, and q is the 'spacial frequency', which is determined by the electrons' scattering angle and wavelength [9]. $A(q)$, the aperture function, models the effect of the objective aperture. The latter minimizes the effect of the objective lens aberrations by limiting the scattering angle of the electrons. This is modeled in the frequency plane by an ideal low pass filter [9]. That is,

$$A(q) = \begin{cases} 1, & |q| < q_a \\ 0, & |q| > q_a, \end{cases} \tag{3}$$

where q_a is a function of the radius of the objective aperture. Finally, $\chi(q,t)$, the aberration function, models the objective lens aberrations and is described in detail in Section III.

Under Assumption 2.1(c), the effect of the specimen over the probe is to modulate the phase of $p(r,t)$ through a transmittance function $\phi(r)$ [8]. Thus, the wave of the electrons that exit the specimen is

$$\psi(r,t) = \phi(r)p(r - r_d, t),$$

where r_d denotes the displacement of the probe from the optical axis imparted by the deflectors. The wave function is then transformed into a diffraction pattern by the LOL and acquired by a detector. Dark field images, the most important kind of images, are acquired by using the ring-shaped HAADF detector in combination with probe scanning and are given by [8]

$$I_{df}(r,t) = \mathfrak{F}^{-1}\{O(q)\} * |p(r,t)|^2,$$

where

$$O(q) \triangleq \int D(\tilde{q})\Phi\left(\tilde{q} + \frac{q}{2}\right)\Phi^{\text{H}}\left(\tilde{q} - \frac{q}{2}\right)d\tilde{q},$$

$D(\tilde{q})$, $\tilde{q} \in \mathbb{R}^2$, is the detector function given by

$$D(\tilde{q}) = \begin{cases} 1, & R_{in} < |\tilde{q}| < R_{out} \\ 0, & \text{otherwise}, \end{cases}$$

$\Phi(q) = \mathfrak{F}\{\phi(r)\}$, and $^{\text{H}}$ denotes complex conjugate.

The quality of a dark field image depends, among other factors, on the microscope alignment. As will be shown shortly, the latter can be controlled using a second type of images called Ronchigrams. These are obtained by shining a static probe through a large objective aperture and projecting the center of the diffraction pattern into a CCD camera. Their intensity, I_{ro}, is given by

$$I_{ro}(q,t) = |\Phi(q) * [P(q,t)\exp(-j\langle q, r_d\rangle)]|^2,$$

where $P(q,t) = \mathfrak{F}\{p(r,t)\}$ and $\langle\cdot,\cdot\rangle$ denotes the inner product in $\mathbb{R}^2$. Finally, probe images, I_{pr}, are important for coordinated position control. These images are obtained by projecting $\psi(r,t)$ onto a screen and are given by

$$I_{pr}(r) = |p(r - r_d, t)|^2. \tag{4}$$

The benefits of using I_{ro} and I_{pr} in STEM control will be evident after the following discussion.

III. STEM Global Procedures

For typical applications, such as measuring the size and shape of catalyst particles [13], the two most important procedures are microscope alignment and coordinated position control. These are described next.

A. Microscope Alignment

Measuring particles or features in the nano-scale requires highly magnified images, whose quality depend critically on the microscope's alignment. The latter involves aligning the electron beam with the optical axis and, more importantly, minimizing the objective lens aberrations (i.e., its deviation from an ideal behavior). Assuming first order (linear) optics, which are valid only for small angular deviations, the aberrations can be expressed solely as a phase shift in the frequency plane characterized by the function $\chi(q,t)$ (see (2)) given by [14]

$$\begin{aligned}\frac{\chi(q,t)}{2\pi} &= \frac{|\mathrm{A}_1(t)|\lambda|q|^2\cos(2\angle q - \angle \mathrm{A}_1(t))}{2} + \frac{C_1(t)\lambda|q|^2}{2} \\ &+ \frac{|\mathrm{A}_2(t)|\lambda^2|q|^3\cos(3\angle q - \angle \mathrm{A}_2(t))}{3} \\ &+ \frac{|\mathrm{B}_2(t)|\lambda^2|q|^3\cos(\angle q - \angle \mathrm{B}_2(t))}{3} + \frac{C_3(t)\lambda^3|q|^4}{4},\end{aligned} \tag{5}$$

where λ is the electrons wavelength, $\mathrm{A}_1(t)$, $\mathrm{A}_2(t)$ and $\mathrm{B}_2(t)$ are complex time-varying coefficients ($|\cdot|$ and $\angle\cdot$ denote magnitude and phase), and $C_1(t)$ and $C_3(t)$ are real time-varying coefficients. The coefficients denote the relative strength of the main aberrations that cause image deformation and limit image resolution: astigmatism, defocus, axial comma, and spherical aberration [11], [13]. Astigmatism is caused by the difference in the lens strength between two perpendicular axes (two-fold astigmatism, $\mathrm{A}_1(t)$) or between three axes separated by $60°$ (three-fold astigmatism, $\mathrm{A}_2(t)$). Defocus, denoted $C_1(t)$ or $\Delta f(t)$, is caused when the probe is brought to focus above (overfocus) or below (underfocus) the specimen plane, i.e., $\Delta f(t) = Z_{ref} - f(t)$. Axial coma, $\mathrm{B}_2(t)$, occurs when the incident beam is not exactly aligned with the optical axis. Finally, the spherical aberration, $C_3(t)$, is caused by the angular difference in the lens strength.

Aligning the microscope requires to measure the aberration coefficients and to adjust the appropriate controls to

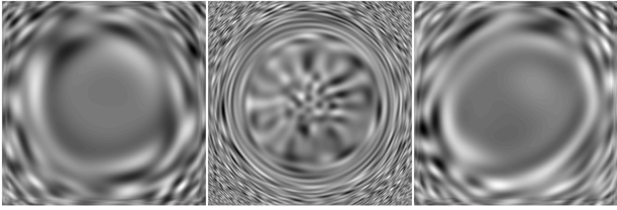

Fig. 2. Simulated Ronchigrams showing the influence of (from left to right) spherical aberration (SA), SA with defocus, SA with two-fold astigmatism.

minimize them. The current available aberration correctors usually measure the coefficients by taking several dark field images under different operating conditions (e.g. different beam orientations), observing the pattern of the changes in the images, and relating those changes to theoretical models of the aberrations [2]–[4]. These correctors, however, assume that the aberration coefficients do not change while the images are acquired, which may not always be the case. Moreover, these correctors are user activated and cannot be used concurrently with normal microscope operations.

A potentially faster alignment procedure can be obtained from Ronchigrams [15], which show features that are directly related to the aberrations. Moreover, since these images are formed by a stationary probe, they may be taken simultaneously with dark field images. Figure 2 shows three simulated Ronchigrams of a thin amorphous specimen considering (from left to right): only spherical aberration (SA), SA and underfocus, and SA with two-fold astigmatism. Note that different aberrations induce different shapes in the Ronchigrams. Unfortunately, measuring the aberrations is not trivial because the low signal-to-noise ratio in the images prevents direct feature extraction. This is further complicated by the transmittance function, $\phi(r)$, when the object is not thin. Two other factors may also limit the use of Ronchigrams. First, Ronchigrams are taken using large objective apertures, while dark field images are taken with small apertures. Hence, the objective apertures need to be switch 'on the fly' for concurrent operation. Second, Ronchigrams are usually taken over amorphous areas of the specimen. Fortunately, recent progress has been made on microscope alignment using Ronchigrams of thin crystalline specimens [16]. This, and a careful mechanical design that minimizes the vibrations induced by the switching the objective apertures, may lead to concurrent alignment control schemes based on Ronchigrams.

B. Coordinated Position Control

This procedure is important for applications where the size and shape of nano-particles must be measured [13]. In such cases, a specimen is first divided into regions. Then, each region is visually surveyed at low magnification to identify areas with high particle concentration. Those areas are subsequently imaged at high magnification and the particles are counted and measured. Note that a large number of particles must be processed in order to reach a statistically significant results, which motivates the need for automation.

The operator usually coordinates by hand the positions of the specimen and the probe. The former is determined by the controls of the goniometer, which is usually actuated by a set of DC servo motors. The position of the probe is determined by the x and y deflectors sets. The x-deflector set is shown in Figure 1. The top coil is excited with a current $i_x(t)$ and deflects the electron beam by $\epsilon_x(t)$ miliradians, where $\epsilon_x(t) \propto i_x(t)$ [9]. The bottom coil is excited with a current $-\alpha_x i_x(t)$ and deflects the beam back by $-\alpha_x \epsilon(t)$ miliradians. α_x is a proportionality constant chosen automatically by the microscope to ensure that the beam crosses the optical axis at the UOL's front focal plane (FFP in Figure 1). This makes it possible to focus the probe on the specimen and form the diffraction pattern at the LOL's back focal plane [11]. For small deflection angles, the net displacement of the probe in the x-direction is then $d_x(t) \propto \epsilon_x(t)$. Similarly, the deflection in the y-direction is $d_y(t) \propto \epsilon_y(t)$. Thus, the total probe displacement, $r_d(t)$, is given by

$$r_d(t) = (\tau_x i_x(t), \tau_y i_y(t)), \tag{6}$$

where τ_x and τ_y are proportionality constants and $i_y(t)$ is the current applied to the y-deflector set.

Coordinating the control of the goniometer and the deflectors presents several challenges. The most severe is the lack of an absolute frame of reference to measure both the position of the specimen and the probe. Moreover, neither position can be measured directly. This is further complicated by the fact that the mechanical coupling between the specimen holder and the deflectors is not perfectly rigid, which introduces additional mechanical alignment errors between these two subsystems. Some of these challenges can be met by developing new detailed physical models and new methods for measuring physical variables in the microscope. For instance, a probe image can be used to determine the probe position (see Section IV). Alternatively, the modeling task can be simplified if visual servo control techniques are used for automatically finding and measuring particles. These techniques, however, require to place the specimen over markers of known size and shape, which may not always be possible.

The new STEM modeling framework is presented next.

IV. STEM Modeling Framework

Two models are introduced here. The first one is suitable for automating the microscope alignment procedure. The second one addresses the coordinated position control problem.

A. Microscope Alignment Model

Consider the model in Figure 3. In this figure, the microscope is seen as the interconnection of three subsystems: the optics, the deflectors and the objective lens. At every time t, the optics subsystem behaves as a linear system (over space) with transfer function $\tilde{P}(q,t) \triangleq P(q,t)\exp(j2\pi\langle q, r_d(t)\rangle)$. It maps the input object function $\Phi(q) = \mathfrak{F}\{\phi(r)\}$ into an output wave function $\Psi(q,t)$. Its output is 'observed' through a nonlinear sensor (a CCD camera or a screen), which produces the observation 'signal' $I_{ro}(q,t)$ (a Ronchigram). $\tilde{P}(q,t)$ is parameterized by the aberration coefficients in (5).

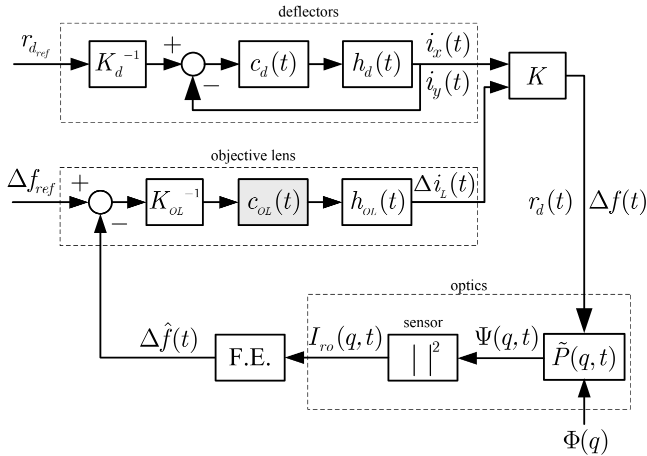

Fig. 3. Model for Ronchigram-based microscope alignment control. The automation goal is to design $c_{OL}(t)$.

Thus, if for simplicity only defocus is considered (as in Figure 3), then

$$\tilde{P}(q,t) = A(q)\exp(j2\pi[\langle q, r_d(t)\rangle + \frac{1}{2}\Delta f(t)\lambda|q|^2]).$$

The deflectors and objective lens subsystems determine $r_d(t)$ and $\Delta f(t)$, respectively. Recall that $r_d(t) = K_d(i_x(t), i_y(t))$, where $K_d = \mathrm{diag}(\tau_x, \tau_y)$ (see (6)). Since $i_x(t)$ and $i_y(t)$ are part of an inductive circuit (the deflector coils), their dynamics can be approximated by a linear second-order model with impulse response $h_d(t)$. This circuit is generally controlled by a local compensator, $c_d(t)$, which keeps $r_d(t)$ constant during the alignment procedure. $\Delta f(t)$ is set by the objective lens subsystem. It is zero when the current in the lens is such that $f(t) = Z_{ref}$. Let i_{ref} denote this current (obtained from Z_{ref} via (1)) and note that small changes in focus values around Z_{ref} are induced by a small changes $\Delta i_L(t)$ of the lens current around i_{ref}. Thus, it can be shown that $\Delta f(t) = K_{OL}\Delta i_L(t)$, where

$$K_{OL} \triangleq \frac{-2U}{\kappa i_{ref}^3}.$$

Note that $\Delta i_L(t)$ is also part of an inductive electrical circuit and possesses linear second-order dynamics, $h_{OL}(t)$. Usually, this circuit is also locally controlled. However, in order to automate the microscope alignment procedure, this local controller must be replaced by a global one, $c_{OL}(t)$. This global controller acts on an error signal generated by comparing the reference defocus value, Δf_{ref}, to an estimate of the actual defocus, $\Delta\hat{f}(t)$. This estimate is in turn generated by a feature extraction (FE) algorithm that processes the Ronchigram image. Finally, note that the optics subsystem and the deflectors and objective lens subsystems are interconnected through the invertible map $K : \mathbb{R}^3 \to \mathbb{R}^2 \times \mathbb{R}$ with action $K(i_x, i_y, \Delta i_L) = (K_d(i_x, i_y), K_{OL}(\Delta i_L))$.

There are two main challenges in applying the scheme described above and designing $c_{OL}(t)$. The first one is related to the validity of K_{OL} and $h_{OL}(t)$. K_{OL} is defined for a particular value of i_{ref} and is only valid for small excursions of this current. For large excursion of the reference current, hysteresis is induced in the current-focus equation

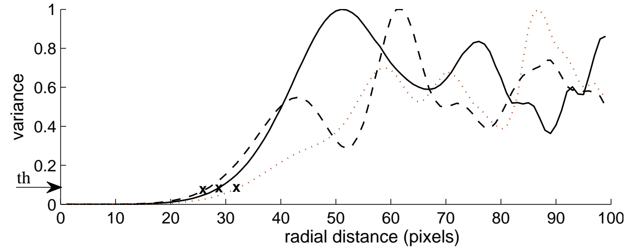

Fig. 4. Rotation variance as a function of pixels' radius for different specimens. The threshold 'th' is used to determine the radius of the Ronchigram central disc, which is a measure of the defocus.

(1) by the magnetization/demagnetization of the objective lens pole pieces [17]. This nonlinear behavior is not yet well characterized and is the subject of current research within the CONDOR project. Likewise, the presence of eddy currents in the objective lens can also modify its dynamics, $h_{OL}(t)$. Thus, more detailed expressions are needed for K_{OL} and $h_{OL}(t)$. The second challenge is to perform feature extraction from images that have low signal-to-noise ratios and large inter-specimen variability. For instance, defocus can be estimated from the radius of a Ronchigram's central disc (a novel method proposed by our group). As shown in Figure 4, the central disc radius can be estimated from the plot of the Ronchigram's rotational variance (which is a function of the pixels' radial distance) by finding the radius at which the variance meets a prescribed threshold 'th'. However, as this figure also shows, this estimate is specimen dependent. To overcome this problem, new analytical estimation methods that are specimen-independent must be developed.

B. Coordinated Position Control Model

As shown in Figure 5, a similar approach is needed for coordinated position control. In this case, the main subsystems to consider are the optics, the specimen holder, and the deflectors. To simplify the description, it will be assumed that the microscope has been properly aligned, so no aberrations are present. It will also be assumed that the specimen can only be displaced in the $x-y$ plane and, as a first approximation, that all the dynamics are linear.

Recall that the specimen is mounted on a goniometer which is actuated by DC servo motors. The dynamics of the goniometer and the motors, $h_g(t)$, are controlled by a compensator, $c_g(t)$, that uses local displacement measurements, $r_g(t)$. Note, however, that the goniometer and the motors are mounted on opposite ends of the rod-shaped specimen holder [11], which is not perfectly rigid (its mechanical dynamics are represented by $h_r(t)$). Thus, the true position of the specimen, $r_{sa}(t)$, may differ from $r_g(t)$. Moreover, the specimen may also be subject to perturbations, $r_p(t)$), such as vibrations or thermal fluctuations. A similar situation is true for the position of the probe, which is specified as a displacement from the center of the optical axis. The frame of reference for this axis is chosen arbitrarily. It can be placed at the tip of the FEG, as shown in Figure 1, or at the center of the objective lens, which is more customary. Unfortunately, any of these frames of reference can be displaced by mechanical vibrations during the microscope's operation. For

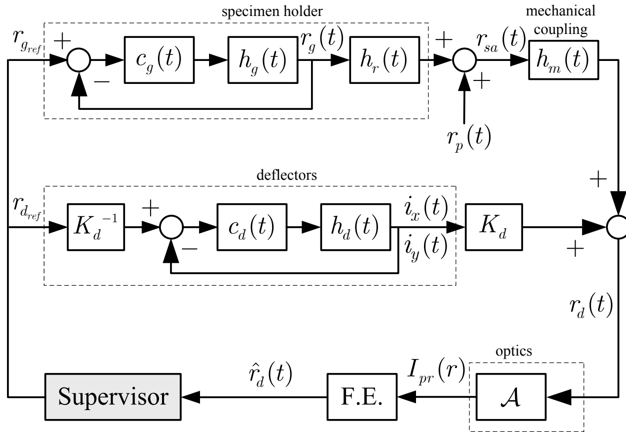

Fig. 5. Model for coordinated position control. The automation goal is to design an appropriate supervisor.

instance, displacing the specimen can induce small vibrations that are transmitted through the microscope's column to the FEG, the objective lens, or the CCD camera, effectively displacing the position of the spot. Even if the mechanical coupling of these subsystems (modeled by $h_m(t)$) were perfectly rigid, the presence of $r_p(t)$ would perturb the probe's position.

Thus, both $r_{sa}(t)$ and $r_d(t)$ must be measured directly. A new method to measure the latter is to estimate it from probe images. Note from (4) that if the microscope is already aligned and the probe is centered at the optical axis, then [9]

$$I_{pr}(r) = |p(r,t)|^2 = \left[\pi q_a^2 \frac{\mathrm{J}_1(2\pi q_a |r|)}{2\pi q_a |r|} \right]^2 ,$$

$\forall r \in \mathbb{R}^2$, where $\mathrm{J}_1(\cdot)$ is the Bessel function (type 1, order 1) and q_a is the aperture function radius (see (3)). Note that this image is *fixed* (it does not depend on $\phi(r)$), circularly symmetric, and centered at the optical axis. Moreover, when the probe is displaced by $r_d(t)$, this image is merely shifted by $r_d(t)$ without distortions. Thus, the optical subsystem can be modeled as a map $\mathcal{A}$ that assigns to each probe position $r_d(t) = \tilde{r}$ an image $\{I_{pr}(r - \tilde{r}), \forall r \in \mathbb{R}^2\}$. Moreover, $r_d(t)$ can be estimated by comparing the current spot image to $\{I_{pr}(r), \forall r \in \mathbb{R}^2\}$ using appropriate feature extraction algorithms. This estimate, $\hat{r}_d(t)$, together with other sensor signals, can then be fed into a supervisory algorithm to automatically coordinate the deflectors and the specimen holder (via $r_{d_{ref}}(t)$ and $r_{g_{ref}}(t)$). Designing this supervisor is central to solving the coordinated position control problem.

Finally, note that two main challenges must be addressed to successfully solve the coordinated position control problem. The first challenge is to identify the mechanical impulse responses $h_r(t)$ and $h_m(t)$, and to understand the nature of the perturbations $r_p(t)$. The second challenge is to add instruments to the STEMs capable of measuring directly the position of the specimen and other physical variables. This is needed in order to design an efficient supervisory algorithm. To this end, it is also important to develop FE algorithms capable of estimating $\hat{r}_d(t)$ from probe images even when strong objective lens aberrations are present.

V. Conclusions

This paper introduced scanning transmission electron microscopy as a new application area for control engineering. STEMs are rather complex machines that present many interesting theoretical and applied control problems. Two of these problems, microscope alignment and coordinated position control, were described in detail and two new models were introduced to analyze them. The steps needed to complete these models were also outlined. Several of them, e.g. the F.E. algorithms, have been recently completed (they will be reported separately) and will be validated in the near future through physical experiments.

Acknowledgements

This research was sponsored by the CONDOR project at FEI company, under the responsibilities of the Embedded Systems Institute (ESI). This project is partially supported by the Dutch Ministry of Economic Affairs under the BSIK program.

References

[1] N. Tanaka, J. Hu, and N. Baba, "An 'on-line' correction method of defocus and astigmatism in HAADF-STEM," *Ultramicroscopy*, vol. 78, no. 1-4, pp. 103–110, 1999.
[2] A. Koster and W. de Ruijter, "Practical autoalignment of transmission electron microscopes," *Ultramicroscopy*, vol. 40, no. 2, pp. 89–107, 1992.
[3] W. Saxton, "A new way of measuring microscope aberrations," *Ultramicroscopy*, vol. 81, no. 2, pp. 41–45, 2000.
[4] N. Baba, K. Terayama, T. Yoshimizu, N. Ichise, and N. Tanaka, "An auto-tuning method for focusing and astigmatism correction in HAADF-STEM, based on the image contrast transfer function," *Journal of Electron Microscopy*, vol. 50, no. 3, pp. 163–176, 2001.
[5] Q. Zheng, M. Braunfeld, J. Sedat, and D. Agard, "An improved strategy for automated electron microscopic tomography," *Journal of Structural Biology*, vol. 147, no. 2, pp. 91–101, 2004.
[6] H. Fujioka, K. Nakamae, K. Ura, S. Takashima, and K. Harasawa, "A Fully Computer-Controlled Scanning Electron Microscope," *Journal of Electron Microscopy*, vol. 35, no. 3, pp. 215–219, 1986.
[7] F. Haguenau, P. Hawkes, J. Hutchison, B. SatiatJeunemaître, G. Simon, and D. Williams, "Key events in the history of electron microscopy," *Microscopy and Microanalysis*, vol. 9, no. 2, pp. 96–138, 2003.
[8] P. Nellist, *Science of Microscopy*. Berlin Heidelberg: Springer Verlag, 2007, ch. 2.
[9] L. Reimer, *Transmission Electron Micrsocopy. Physics of Image Formation and Microanalysis*, 3rd ed. Berlin Heidelberg: Springer Verlag, 1993.
[10] M. D. Graef, *Introduction to Conventional Transmission Electron Microscopy*. Cambridge: Cambridge University Press, 2003.
[11] D. Williams and C. Carter, *Transmission Electron Microscopy, A Textbook for Materials Science*. New York: Plenum Press, 1996.
[12] P. W. Hawkes and E. Kasper, *Principle of Electron Optics. Volume 3. Wave Optics*. London, UK: Academic Press, 1994.
[13] A. Datye and D. Smith, "The study of heterogeneous catalysts by high-resolution transmission electron microscopy," *Catalysis Reviews*, vol. 34, no. 1, pp. 129–178, 1992.
[14] R. Meyer, A. Kirkland, and W. Saxton, "A new method for the determination of the wave aberration function for high-resolution TEM. 2. Measurement of the antisymmetric aberrations," *Ultramicroscopy*, vol. 99, no. 2-3, pp. 115–123, 2004.
[15] J. Rodenburg and E. Macak, "Optimising the resolution of TEM/STEM with the electron ronchigram," *Microscopy and Analysis*, vol. 16, no. 2, pp. 5–7, July 2002.
[16] Q. Ramasse and A. Bleloch, "Diagnosis of aberrations from crystalline samples in scanning transmission electron microscopy," *Ultramicroscopy*, vol. 106, no. 1, pp. 37–56, 2005.
[17] J. T. L. Thong and F. Li, "Eddy current compensation for magnetic electron lenses," *Measurement Science and Technology*, vol. 7, no. 11, pp. 1583–1590, 1996.